

# A parametric tensor ROM for the shallow water dam break problem

Md Rezwan Bin Mizan <sup>\*</sup> Maxim Olshanskii <sup>†</sup> Ilya Timofeyev<sup>‡</sup>

## Abstract

We develop a variant of a tensor reduced-order model (tROM) for the parameterized shallow-water dam-break problem. This hyperbolic system presents multiple challenges for model reduction, including a slow decay of the Kolmogorov  $N$ -width of the solution manifold, shock formation, and the loss of smooth solution dependence on parameters. These issues limit the performance of traditional Proper Orthogonal Decomposition based ROMs. Our tROM approach, based on a low-rank tensor decomposition, builds a parameter-to-solution map from high-fidelity snapshots and constructs localized reduced bases via a local POD procedure. We apply this method to both dry-bed and wet-bed problem setups, showing that the non-interpolatory variant of the tROM, combined with Chebyshev sampling near critical parameter values, effectively captures parameter-dependent behavior and significantly outperforms standard POD-ROMs. This is especially evident in the wet-bed case, where POD-ROMs exhibit poor resolution of shock waves and spurious oscillations.

## 1 Introduction

The development of accurate and efficient Reduced-Order Models (ROMs) that capture parametric variations in numerical simulations of time-dependent partial differential equations (PDEs) remains a major challenge in scientific computing. This task is typically problem-dependent and often necessitates adaptations of established techniques. The challenge becomes particularly acute when the parameter vector is high-dimensional. Among the most prominent approaches are traditional Proper Orthogonal Decomposition (POD)-based ROMs, which have seen many successful applications [3].

However, the efficiency of many traditional ROMs is theoretically constrained by the decay rate of the Kolmogorov  $N$ -width of the solution manifold for the parametric problem of interest. The Kolmogorov  $N$ -width quantifies how well a manifold can be approximated by an  $N$ -dimensional linear subspace. While sharp estimates of the Kolmogorov  $N$ -width are rare [19, 14], its equivalence to the best  $N$ -term approximation in greedy POD [5] suggests exponential or algebraic decay for parabolic and elliptic problems with sufficiently smooth parametric dependence; see, e.g., [10, 6, 9, 13, 2].

In contrast, hyperbolic problems often exhibit much slower decay rates. For example, for linear problems with discontinuous initial data, the authors in [21, 12] observed a decay rate of  $O(N^{-1/2})$ . This slower decay implies that a relatively high-dimensional subspace is required for accurate solution approximation. This partially explains why POD-based ROMs for hyperbolic problems are comparatively less developed; see, however, [26, 11, 1, 7].

---

<sup>\*</sup>Dept. of Mathematics, University of Houston, Houston, TX 77204, mbinmiza@cougarnet.uh.edu

<sup>†</sup>Dept. of Mathematics, University of Houston, Houston, TX 77204, maolshanskiy@uh.edu

<sup>‡</sup>Dept. of Mathematics, University of Houston, Houston, TX 77204, itimofey@cougarnet.uh.edu

The situation becomes even more complex for nonlinear hyperbolic problems due to the formation of shocks, which require accurate tracking. The Shallow Water Equations (SWE), addressed in this study, provide a classical example of such a problem. To overcome the limitations of linear reduction techniques, machine learning (ML) methods have been employed to construct ROMs for hyperbolic systems; see, e.g., [11, 1, 7]. ML-based reduced models for the SWE include [25, 4, 24]. However, ML approaches have their own limitations, particularly the lack of a mature theoretical foundation.

A more mathematically grounded alternative is the tensor ROM (tROM) approach [16, 17, 22], developed recently to address the limitations of POD-based ROMs for parametric PDEs. This method is especially well-suited to time-dependent PDEs with high-dimensional parameter spaces [16]. The tROM is a projection-based method that performs high-fidelity simulations across different parameter values to construct an  $(N + D)$ -dimensional “snapshot” tensor in a low-rank tensor format, where  $N$  is the physical dimension and  $D$  is the number of parameters. This tensor represents a discrete approximation of the parameter-to-solution map. By operating directly on these low-rank structures, one can compute a parameter-dependent reduced basis for any new parameter value. Further details are given in Section 2.2.1.

In this work, we employ a Low-Rank Tensor Decomposition (LRTD) in the Tucker format to build a tROM and distinguish between interpolatory and non-interpolatory variants. For interpolatory tROMs, a local reduced basis is computed via low-rank interpolation of the parameter-to-solution map. In the non-interpolatory case, interpolation is replaced by a local POD procedure. As we shall demonstrate, the non-interpolatory tROM performs better.

We apply the tensor ROM approach to a hyperbolic problem – specifically, the one-dimensional SWE dam-break problem with both dry-bed and wet-bed initial conditions. The initial conditions are characterized by the parameters  $(h_L, h_R)$ , representing the water heights to the left and right of the dam, respectively. Hence, the parameter space has dimension  $D = 2$ . The dry-bed case ( $h_R = 0$ ) leads to a relatively simple solution involving a rarefaction wave. In contrast, the wet-bed case ( $h_R > 0$ ) is more challenging due to the formation of a shock wave downstream of the dam. For this case, the shock persists for all times  $t > 0$ , and the derivative of the solution with respect to  $h_R$  near the shock becomes unbounded as  $h_R \rightarrow 0$ . This makes the construction of projection-based ROMs particularly difficult, as the quality of approximation hinges on the regularity of the parameter-to-solution map [18]. Thus, even though the physical and parameter dimensions of the problem are low, *the hyperbolic nature of the problem, shock formation and the lack of regularity near  $h_R = 0$  poses a significant challenge for ROM development.*

We demonstrate that the non-interpolatory tROM, combined with Chebyshev sampling in the wet-bed parameter direction, is an effective strategy. Although the resulting local reduced spaces have higher dimensions than those typically required for parabolic or elliptic problems, this is consistent with the known slow decay of the Kolmogorov  $N$ -width in hyperbolic settings. We also show that this method significantly outperforms standard POD-ROMs, especially in the wet-bed case, where POD-ROMs struggle to resolve shock waves and tend to generate spurious high-frequency oscillations.

The remainder of the paper is organized as follows. In Section 2, we present the governing equations, describe the projection-based ROM approach, and provide an overview of tROM and POD-ROM techniques. For further details on tROMs, we refer the reader to [16, 17]. Section 3 presents numerical results for both dry-bed and wet-bed cases, including an analysis of local basis generation thresholds, variation in parameter  $h_R$ , and a performance comparison between interpolatory and non-interpolatory tROMs as well as between POD-ROM and tROM. Finally, in Appendix A, we discuss the solution regularity of the wet-bed dam-break problem near the

dry-bed limit.

## 2 Methods and Setup

In this section, we briefly describe the shallow-water equations and the formalism for developing Reduced-Order Models. In particular, we outline the standard POD-ROM approach and discuss a tensor ROM.

### 2.1 Problem Formulation

We consider the one-dimensional (1D) shallow water equations (SWEs) to model the dam-break problem, a classical benchmark for hyperbolic conservation laws. The dam-break scenario involves a sudden release of water, generating shock and rarefaction waves, making it an ideal test case for numerical methods and reduced-order modeling of hyperbolic systems.

**Governing Equations.** In conservative form, without source terms, the 1D SWEs are expressed as:

$$\partial_t \mathbf{U} + \partial_x \mathbf{F} = \mathbf{0}, \quad (1)$$

with

$$\mathbf{U} = \begin{bmatrix} h \\ q \end{bmatrix}, \quad \mathbf{F} = \begin{bmatrix} q \\ q^2/h + \frac{1}{2} g h^2 \end{bmatrix},$$

where  $h(x, t)$  is the water depth,  $q(x, t) = h u$  the discharge,  $u(x, t)$  the depth-averaged velocity, and  $g$  gravity.

**Full-order model.** Full-order model (FOM) solutions to equation (1) are computed using a standard finite volume discretization outlined below. In time we apply a second-order accurate explicit Heun (RK-2) scheme, while spatial fluxes use the local Lax–Friedrichs (LLF) formula

$$\mathbf{F}_{i+\frac{1}{2}} = \frac{1}{2} [\mathbf{F}(\mathbf{U}_i) + \mathbf{F}(\mathbf{U}_{i+1})] - \frac{\lambda_{i+\frac{1}{2}}}{2} (\mathbf{U}_{i+1} - \mathbf{U}_i), \quad (2)$$

with maximum wave speed  $\lambda_{i+\frac{1}{2}} = \max(|u_i| + c_i, |u_{i+1}| + c_{i+1})$ ,  $c_i = \sqrt{g h_i}$ . A constant time step  $\Delta t$  is chosen such that the CFL condition  $\max_i \lambda_{i+\frac{1}{2}} \Delta t / \Delta x < 1$  holds; simulations advance to a prescribed final time  $T$ . The computational domain is  $[0, L_x]$ , with  $L_x = 100$ , discretized using a uniform grid with  $N_x$  interior points plus two ghost points (one at each end). The spatial step size is  $\Delta x = L_x / N_x$ , with interior points at  $x_i = i \Delta x$  ( $i = 1, \dots, N_x$ ), and ghost points at  $x_0 = -\Delta x / 2$ ,  $x_{N_x+1} = L_x + \Delta x / 2$ .

**Parametrized initial conditions.** Placing a depth discontinuity at  $x_{\text{dam}} = L_x / 2$  gives

$$h(x, 0) = \begin{cases} h_L, & x < x_{\text{dam}}, \\ h_R, & x \geq x_{\text{dam}}, \end{cases} \quad q(x, 0) = 0, \quad (3)$$

with  $h_L > h_R \geq 0$ . These depths form the parameter vector  $\boldsymbol{\mu} = (h_L, h_R) \in \mathcal{P} \subset \mathbb{R}^2$ . Our parameter domain is a box  $\mathcal{P} = [h_L^{\min}, h_L^{\max}] \times [h_R^{\min}, h_R^{\max}]$ . The setups with  $h_R = 0$  and  $h_R > 0$  are known as the *dry-bed* and *wet-bed* dam break problem, respectively.

**Boundary conditions.** We impose outflow boundary conditions by copying the nearest interior state to each ghost cell, equivalent to  $\partial_x h = \partial_x q = 0$  at  $x = 0, L_x$ .

**Parameters sampling.** Snapshots are collected on a two-parameter grid. The dam depths are sampled uniformly:

$$h_L^i = h_L^{\min} + \frac{(h_L^{\max} - h_L^{\min})(i-1)}{N_L - 1}, \quad i = 1, \dots, N_L, \quad (4)$$

while for the downstream bed depths we use  $N_R$  uniformly distributed or Chebyshev nodes:

$$h_R^j = \frac{1}{2} \left[ (h_R^{\min} + 2h_R^{\max}) - (2h_R^{\max} - h_R^{\min}) \cos\left(\frac{\pi j}{2(N_R-1)}\right) \right], \quad j = 1, \dots, N_R - 1. \quad (5)$$

For every  $(h_L, h_R)$  pair we store snapshots of  $h$  and  $q$  at all  $N_x$  interior cells at regular time intervals. We use  $(h_L^{\min}, h_L^{\max}) = (10, 28)$  and  $(h_R^{\min}, h_R^{\max}) = (0, 8)$  in this paper, which is significantly larger comparing to other studies of the parametrized dam-break problem known from the literature [8, 15, 20, 23, 26, 27].

## 2.2 Reduced-Order Modeling

Reduced-order modeling constructs low-dimensional approximations of high-dimensional systems to enable efficient simulations while preserving the dominant dynamics of the full-order model. For the 1D dam-break problem governed by the SWEs, the ROMs facilitate rapid exploration of parametric variations in initial conditions, such as left and right water heights, denoted by the parameter vector  $\boldsymbol{\mu} = (h_L, h_R)$ . This section outlines the principles of ROM, introduces tROM using the LRTD with Tucker format, and details the interpolatory and non-interpolatory tROM approaches employed. Additionally, the POD ROM is discussed for comparison, and implementation details highlight the offline-online strategy that enhances computational efficiency.

A projection ROM approximates the discrete solutions  $h^n, q^n \in \mathbb{R}^{N_x}$  at each time level by

$$h^n \approx V_h^{\ell_h}(\boldsymbol{\mu}) \boldsymbol{\alpha}_h^n, \quad q^n \approx V_q^{\ell_q}(\boldsymbol{\mu}) \boldsymbol{\alpha}_q^n, \quad (6)$$

where  $V_h^{\ell_h}(\boldsymbol{\mu}) \in \mathbb{R}^{N_x \times \ell_h}$ ,  $V_q^{\ell_q}(\boldsymbol{\mu}) \in \mathbb{R}^{N_x \times \ell_q}$  are orthonormal bases in  $\ell_h$ -dimensional and  $\ell_q$ -dimensional ROM spaces, respectively, possibly dependent on  $\boldsymbol{\mu}$  where  $\ell_h \ll N_x$  and  $\ell_q \ll N_x$ . The coefficients  $\boldsymbol{\alpha}_h^n \in \mathbb{R}^{\ell_h}$  and  $\boldsymbol{\alpha}_q^n \in \mathbb{R}^{\ell_q}$  evolve in time. Galerkin projection of the FOM onto these subspaces is given by

$$\begin{aligned} (V_h^{\ell_h})^T \left( \frac{h^{n+1} - h^n}{\Delta t} + \frac{1}{\Delta x} (\mathbf{F}_{h,i+\frac{1}{2}}^n - \mathbf{F}_{h,i-\frac{1}{2}}^n) \right) &= \mathbf{0}, \\ (V_q^{\ell_q})^T \left( \frac{q^{n+1} - q^n}{\Delta t} + \frac{1}{\Delta x} (\mathbf{F}_{q,i+\frac{1}{2}}^n - \mathbf{F}_{q,i-\frac{1}{2}}^n) \right) &= \mathbf{0}, \end{aligned} \quad (7)$$

where  $\mathbf{F}_{h,i+\frac{1}{2}}^n$  and  $\mathbf{F}_{q,i+\frac{1}{2}}^n$  are the interface fluxes evaluated midway through the RK-2 step.

Initial conditions are also needs to be projected,  $\boldsymbol{\alpha}_h^0 = (V_h^{\ell_h})^T h^0$ ,  $\boldsymbol{\alpha}_q^0 = (V_q^{\ell_q})^T q^0$ .

The core challenge lies in constructing parameter-specific subspaces  $V_h^{\ell_h}(\boldsymbol{\mu})$  and  $V_q^{\ell_q}(\boldsymbol{\mu})$ . The tROM exploits the space–time–parameter structure of snapshot data, offering superior adaptability compared to the global POD bases.

### 2.2.1 Tensor ROM

Tensor ROM enhances projection-based ROM by organizing snapshot data into a higher-order tensor, preserving the intrinsic structure across spatial, temporal, and parametric dimensions.

Unlike classical POD, which flattens snapshots into a matrix, tROM employs LRTD to compress data and generate parameter-adaptive bases, making it well-suited for problems with a parametric variability, such as the dam-break problem with its shock fronts.

In tROM, the goal is to approximate solutions in low-dimensional subspaces  $V_h^{\ell_h}(\boldsymbol{\mu}), V_q^{\ell_q}(\boldsymbol{\mu}) \subset \mathbb{R}^{N_x}$ , where  $\ell_h, \ell_q \ll N_x$ , tailored to a parameter  $\boldsymbol{\mu} \in \mathcal{D}$ . The snapshot set, comprising FOM solutions  $\{h(\mathbf{x}, t_n; \boldsymbol{\mu}_k), q(\mathbf{x}, t_n; \boldsymbol{\mu}_k)\}_{n,k}$  for time steps  $t_n$  and parameter samples  $\boldsymbol{\mu}_k \in \mathcal{D}$ , is organized into 4-D tensors  $\mathcal{Q}_h, \mathcal{Q}_q \in \mathbb{R}^{N_x \times N_{\mu_1} \times N_{\mu_2} \times N_T}$ , where  $N_{\mu_1}, N_{\mu_2}$  are the number of samples for  $h_L$  and  $h_R$ , and  $N_T$  is the number of temporal snapshots.

**LRTD** We adopt the Tucker decomposition, a multilinear LRTD method, to approximate the snapshot tensors. For the water-depth tensor, the approximation is

$$\mathcal{Q}_h \approx \tilde{\mathcal{Q}}_h = \mathcal{G}_h \times_1 \mathbf{W}_h \times_2 \boldsymbol{\Sigma}_h^{(1)} \times_3 \boldsymbol{\Sigma}_h^{(2)} \times_4 \mathbf{V}_h, \quad (8)$$

where  $\mathcal{G}_h \in \mathbb{R}^{\tilde{N}_x \times \tilde{N}_{\mu_1} \times \tilde{N}_{\mu_2} \times \tilde{N}_T}$  is the core tensor,  $\mathbf{W}_h \in \mathbb{R}^{N_x \times \tilde{N}_x}$ ,  $\boldsymbol{\Sigma}_h^{(1)} \in \mathbb{R}^{N_{\mu_1} \times \tilde{N}_{\mu_1}}$ ,  $\boldsymbol{\Sigma}_h^{(2)} \in \mathbb{R}^{N_{\mu_2} \times \tilde{N}_{\mu_2}}$ , and  $\mathbf{V}_h \in \mathbb{R}^{N_T \times \tilde{N}_T}$  are orthogonal factor matrices;  $\tilde{N}_x, \tilde{N}_{\mu_1}, \tilde{N}_{\mu_2}, \tilde{N}_T$  are reduced ranks ( $\tilde{N}_x \ll N_x$ ). The operator  $\times_m$  denotes mode- $m$  tensor-matrix multiplication. The approximation error is controlled by a tolerance  $\epsilon_h$ :

$$\|\mathcal{Q}_h - \tilde{\mathcal{Q}}_h\|_F \leq \epsilon_h \|\mathcal{Q}_h\|_F. \quad (9)$$

The columns of the spatial factor matrix  $\mathbf{W}_h$  spans a universal subspace:

$$V_{\text{univ},h} = \text{span}\{\mathbf{W}_h[:, m]\}_{m=1}^{\tilde{N}_x} \subset \mathbb{R}^{N_x}, \quad (10)$$

representing information given by all collected snapshots up to the LRTD error. The parameter factor matrices  $\boldsymbol{\Sigma}_h^{(1)}, \boldsymbol{\Sigma}_h^{(2)}$  encode parametric dependencies, enabling the construction of local bases for unseen parameters.

### 2.2.2 Interpolatory tROM

The interpolatory tROM [16, 17] generates parameter-specific bases by interpolating the parameter factor matrices. For an parameter  $\boldsymbol{\mu}^* = (h_L^*, h_R^*)$ , not necessarily from a sampling set, the online phase constructs interpolation vectors using Lagrange interpolation of order  $p$ :

$$\chi_{p,L}(h_L^*)_k = \begin{cases} \prod_{\substack{m=1 \\ m \neq k}}^p \frac{h_L^{(i_m)} - h_L^*}{h_L^{(i_m)} - h_L^{(k)}} & \text{if } k = i_k \in \{i_1, \dots, i_p\}, \\ 0 & \text{otherwise,} \end{cases} \quad (11)$$

and similarly for  $\chi_{p,R}(h_R^*)$ , selecting the  $p$  closest sampled parameters  $h_L^{(i_m)}, h_R^{(i_m)}$ . The local core matrix is formed by contracting the core tensor:

$$\mathcal{C}_h(\boldsymbol{\mu}^*) = \mathcal{G}_h \times_2 \chi_{p,L}(h_L^*) \times_3 \chi_{p,R}(h_R^*) \in \mathbb{R}^{\tilde{N}_x \times \tilde{N}_T}, \quad (12)$$

followed by an SVD:  $\mathcal{C}_h(\boldsymbol{\mu}^*) = \hat{U}_h \boldsymbol{\Sigma}_h \hat{V}_h^T$ . The local basis is then given by

$$V_h^{\ell_h}(\boldsymbol{\mu}^*) = \mathbf{W}_h \hat{U}_h[:, 1 : \ell_h] \subset V_{\text{univ},h}, \quad (13)$$

where  $\ell_h$  is chosen based on a local energy threshold  $\epsilon_{\text{loc}}$ . The process is analogous for  $V_q^{\ell_q}(\boldsymbol{\mu}^*)$ .

### 2.2.3 Non-Interpolatory tROM

The non-interpolatory tROM [22] constructs local bases by combining snapshot data from several nearest parameter grid points (four points are taken in our implementation), avoiding interpolation to enhance accuracy for discontinuous solutions. For  $\boldsymbol{\mu}^*$ , the method identifies bracketing indices such that  $h_L^{(k_{\text{low}})} \leq h_L^* < h_L^{(k_{\text{high}})}$  and  $h_R^{(l_{\text{low}})} \leq h_R^* < h_R^{(l_{\text{high}})}$ . Reduced tensors are computed:

$$\begin{aligned} C_{h,1} &= \mathcal{G}_h \times_2 \boldsymbol{\Sigma}_h^{(1)}[k_{\text{low}}, :] \times_3 \boldsymbol{\Sigma}_h^{(2)}[l_{\text{low}}, :], \\ C_{h,2} &= \mathcal{G}_h \times_2 \boldsymbol{\Sigma}_h^{(1)}[k_{\text{low}}, :] \times_3 \boldsymbol{\Sigma}_h^{(2)}[l_{\text{high}}, :], \\ C_{h,3} &= \mathcal{G}_h \times_2 \boldsymbol{\Sigma}_h^{(1)}[k_{\text{high}}, :] \times_3 \boldsymbol{\Sigma}_h^{(2)}[l_{\text{low}}, :], \\ C_{h,4} &= \mathcal{G}_h \times_2 \boldsymbol{\Sigma}_h^{(1)}[k_{\text{high}}, :] \times_3 \boldsymbol{\Sigma}_h^{(2)}[l_{\text{high}}, :], \end{aligned} \tag{14}$$

forming a matrix  $C_h = [C_{h,1}, C_{h,2}, C_{h,3}, C_{h,4}]$ . An SVD  $C_h = \widehat{U}_h \boldsymbol{\Sigma}_h \widehat{V}_h^T$  yields the basis as in (13), with rank  $\ell_h$  set by  $\epsilon_{\text{loc}}$ . The process is repeated for  $q$ .

### 2.2.4 POD-ROM

The POD-ROM constructs global bases using matrix SVD, offering a simpler but less adaptive alternative. Snapshots are organized into matrices  $X_h, X_q \in \mathbb{R}^{N_x \times (N_{\mu_1} N_{\mu_2} N_T)}$ , and truncated SVD is applied:

$$X_h \approx U_h \boldsymbol{\Sigma}_h V_h^T, \quad X_q \approx U_q \boldsymbol{\Sigma}_q V_q^T, \tag{15}$$

where  $V_h = U_h[:, 1 : \ell_h]$ ,  $V_q = U_q[:, 1 : \ell_q]$  are the leading POD modes, selected to retain at least a  $1 - \epsilon_{\text{POD}}$  fraction of the total energy

### 2.2.5 Implementation

The tROM and POD-ROM employ an offline–online strategy to balance computational effort.

#### Offline Stage

- (O1) **Snapshot Generation:** Solve the FOM over the parameter grid, storing snapshots at selected time steps in tensors  $\mathcal{Q}_h, \mathcal{Q}_q$  (tROM) or matrices  $X_h, X_q$  (POD).
- (O2) **Compression:** For tROM, apply truncated Higher-Order SVD (HOSVD) to  $\mathcal{Q}_h, \mathcal{Q}_q$ , yielding core tensors and factor matrices with tolerances  $\epsilon_h, \epsilon_q$ . For POD, perform SVD on  $X_h, X_q$ , obtaining global bases with threshold  $\epsilon_{\text{POD}}$ .

#### Online Stage

- (N1) **Basis Construction:** Given a new parameter  $\boldsymbol{\mu}^* = (h_L^*, h_R^*)$ ,
  - *Interpolatory tROM:* Compute the local core via (12), perform its thin SVD, and assemble  $V_h^{\ell_h}(\boldsymbol{\mu}^*), V_q^{\ell_q}(\boldsymbol{\mu}^*)$  using (13) with  $\epsilon_{\text{loc}}$ .
  - *Non-Interpolatory tROM:* Form the four reduced cores from (14), concatenate them into  $C_h$  (and  $C_q$ ), compute its thin SVD, and assemble  $V_h^{\ell_h}(\boldsymbol{\mu}^*), V_q^{\ell_q}(\boldsymbol{\mu}^*)$  via (13) with  $\epsilon_{\text{loc}}$ .
  - *POD-ROM:* Reuse the precomputed global bases  $V_h = U_h[:, 1 : \ell_h]$ ,  $V_q = U_q[:, 1 : \ell_q]$ .
- (N2) **Reduced Operator Projection:** Project the precomputed flux operators onto the local bases  $V_h^{\ell_h}(\boldsymbol{\mu}^*), V_q^{\ell_q}(\boldsymbol{\mu}^*)$  (tROM) or onto  $V_h, V_q$  (POD).

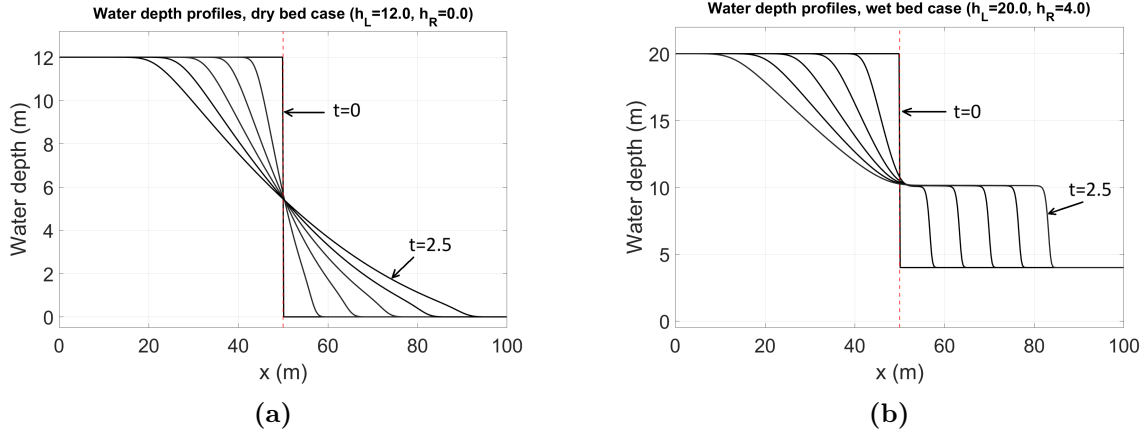


**Figure 1:** Water depth profiles evolution in time for the cases of dry and wet bed. Snapshots are shown every  $\Delta t = 0.5$ . Click the plots for full animation.

(N3) **Time Integration:** Integrate the reduced system (7) (using Heun’s RK-2) in the chosen low-dimensional basis, and reconstruct  $h^n = V_h^{\ell_h}(\boldsymbol{\mu}^*) \boldsymbol{\alpha}_h^n$ ,  $q^n = V_q^{\ell_q}(\boldsymbol{\mu}^*) \boldsymbol{\alpha}_q^n$  (or analogous POD form) when required.

### 3 Numerical Experiments

A typical evolution of the water depth for the cases of dry and wet beds is illustrated in Figure 1, which shows snapshots of the computed FOM solutions for  $h_L = 12$  (dry bed) and  $h_L = 20$ ,  $h_R = 4$  (wet bed). Note that the evolution differs significantly between the dry-bed and wet-bed cases. In the dry-bed case, we observe the formation of a sharp front (dry–wet interface) that moves into the initially dry downstream region, with the water depth decreasing smoothly from the dam location to zero at the front edge. A rarefaction wave forms and propagates upstream. This FOM solution approximates the self-similar profiles given by (19), with the front speed given by  $2\sqrt{gh_L}$ ; see Eq. (22).

In contrast, in the wet-bed case, the initial discontinuity between  $h_L$  and  $h_R$  generates a shock wave. The height and speed of the wave depend on the ratio  $h_L/h_R$ . Both rarefaction and shock structures evolve smoothly; their speed and position can be determined analytically by solving the system of algebraic equations (20)–(21).

#### 3.1 Tensor ROM performance

Let  $u_{\text{FOM}}(x, t; \boldsymbol{\mu})$  and  $u_{\text{ROM}}(x, t; \boldsymbol{\mu})$  denote the full-order and reduced-order solutions of the dam-break problem on the spatial domain  $\Omega = [0, L_x]$  and the time interval  $[0, T]$ , where  $\boldsymbol{\mu} = (h_L, h_R)$  is a vector of physical parameters.

The error function for a given parameter value is defined as

$$e(x, t; \boldsymbol{\mu}) = u_{\text{ROM}}(x, t; \boldsymbol{\mu}) - u_{\text{FOM}}(x, t; \boldsymbol{\mu}).$$

We are interested in the *space-time* relative error in the  $L^2(0, T; L^2(\Omega))$  norm, given by

$$E_{L^2(L^2)}(\boldsymbol{\mu}) = \frac{\left( \int_0^T \|e(\cdot, t, \boldsymbol{\mu})\|_{L^2(\Omega)}^2 dt \right)^{\frac{1}{2}}}{\left( \int_0^T \|u_{\text{FOM}}(\cdot, t, \boldsymbol{\mu})\|_{L^2(\Omega)}^2 dt \right)^{\frac{1}{2}}}. \quad (16)$$

Similarly, the relative error in the  $L^2(0, T; H^1(\Omega))$  norm is denoted by  $E_{L^2(H^1)}(\boldsymbol{\mu})$ .

Let  $I_R = [h_R^{\min}, h_R^{\max}]$  and  $I_L = [h_L^{\min}, h_L^{\max}]$ . For a fixed  $h_L$ , the maximum and average errors over the wet-bed water height parameter  $h_R$  are defined as

$$E_{L^2(L^2)}^{\text{sup}}(h_L) = \sup_{h_R \in I_R} E_{L^2(L^2)}(\cdot, h_R), \quad E_{L^2(L^2)}^{\text{avr}}(h_L) = \int_{I_R} E_{L^2(L^2)}(\cdot, h_R) dh_R, \quad (17)$$

with analogous definitions for  $E_{L^2(H^1)}^{\text{sup}}(h_L)$  and  $E_{L^2(H^1)}^{\text{avr}}(h_L)$ .

Finally, the maximum and average errors over the entire parameter domain  $\Omega_\mu = I_L \times I_R$  are given by

$$E_{L^2(L^2)}^{\text{sup}} = \sup_{\boldsymbol{\mu} \in \Omega_\mu} E_{L^2(L^2)}(\boldsymbol{\mu}), \quad E_{L^2(L^2)}^{\text{avr}} = \int_{\Omega_\mu} E_{L^2(L^2)}(\boldsymbol{\mu}) d\boldsymbol{\mu}. \quad (18)$$

The same definitions apply to the maximum and average errors in the  $L^2(0, T; H^1(\Omega))$  norm. In practice, these quantities were computed using a Monte Carlo procedure with random sampling of  $\Omega_\mu$ .

### 3.1.1 Effect of local threshold on tROM performance

We start the assessment of tROM by examining the effect of varying the local threshold  $\epsilon_{\text{loc}}$  for parameter-specific basis generation in the online phase of our tensor reduced-order model.

We test two cases with  $N_L = 13$ ,  $N_R = 17$ ,  $h_L = 27$  m, and  $h_R \in \{0.14, 3.00\}$  m, varying  $\epsilon_{\text{loc}} \in \{4.0 \times 10^{-2}, 1.0 \times 10^{-2}, 4.0 \times 10^{-3}, 1.0 \times 10^{-3}\}$ . Water-depth profiles, errors, and ROM dimensions for each  $h_R$  are plotted in Figure 2, with zoom-ins highlighting shock-front differences.

The results reveal an expected trade-off: smaller  $\epsilon_{\text{loc}}$  enhances the non-interpolatory tROM's accuracy by retaining more basis vectors, thereby reducing errors but increasing ROM dimensions and computational cost, with notably improved shock-front resolution for  $h_R = 0.14$  m due to its sharper discontinuity. From Figure 2, we observe that  $\epsilon_{\text{loc}} = 4.0 \times 10^{-3}$  performs reasonably well and offers a good balance between accuracy and efficiency (i.e., ROM dimension). Thus, we fix  $\epsilon_{\text{loc}} = 4.0 \times 10^{-3}$  for all remaining experiments (unless explicitly stated otherwise) to ensure consistent performance across varying conditions.

### 3.1.2 Impact of wet-bed water depth

We now study the effect of varying  $h_R$  on the accuracy and ROM dimensions of the tensor reduced-order model. To this end, we fix  $h_L = 25$  m,  $N_L = 13$ ,  $N_R = 17$ , and  $\epsilon_{\text{loc}} = 4.0 \times 10^{-3}$  (as it was found to be close to optimal), and evaluate the  $E_{L^2(L^2)}(h_L)$  and  $E_{L^2(H^1)}(h_L)$  errors along with the ROM dimensions  $\ell_h$  and  $\ell_q$ . Next, we fix the ROM dimensions at  $\ell_h = 30$ ,  $\ell_q = 50$ , instead of using  $\epsilon_{\text{loc}}$ , and assess performance for varying  $h_R$ .

Results for both cases (fixed  $\epsilon_{\text{loc}}$  and adaptive ROM dimensions and fixed ROM dimensions) are reported in Table 2. For the adaptive ROM case, we observe that the ROM accuracy varies only slightly across the range of wet-bed water depths, with the resulting ROM dimensions

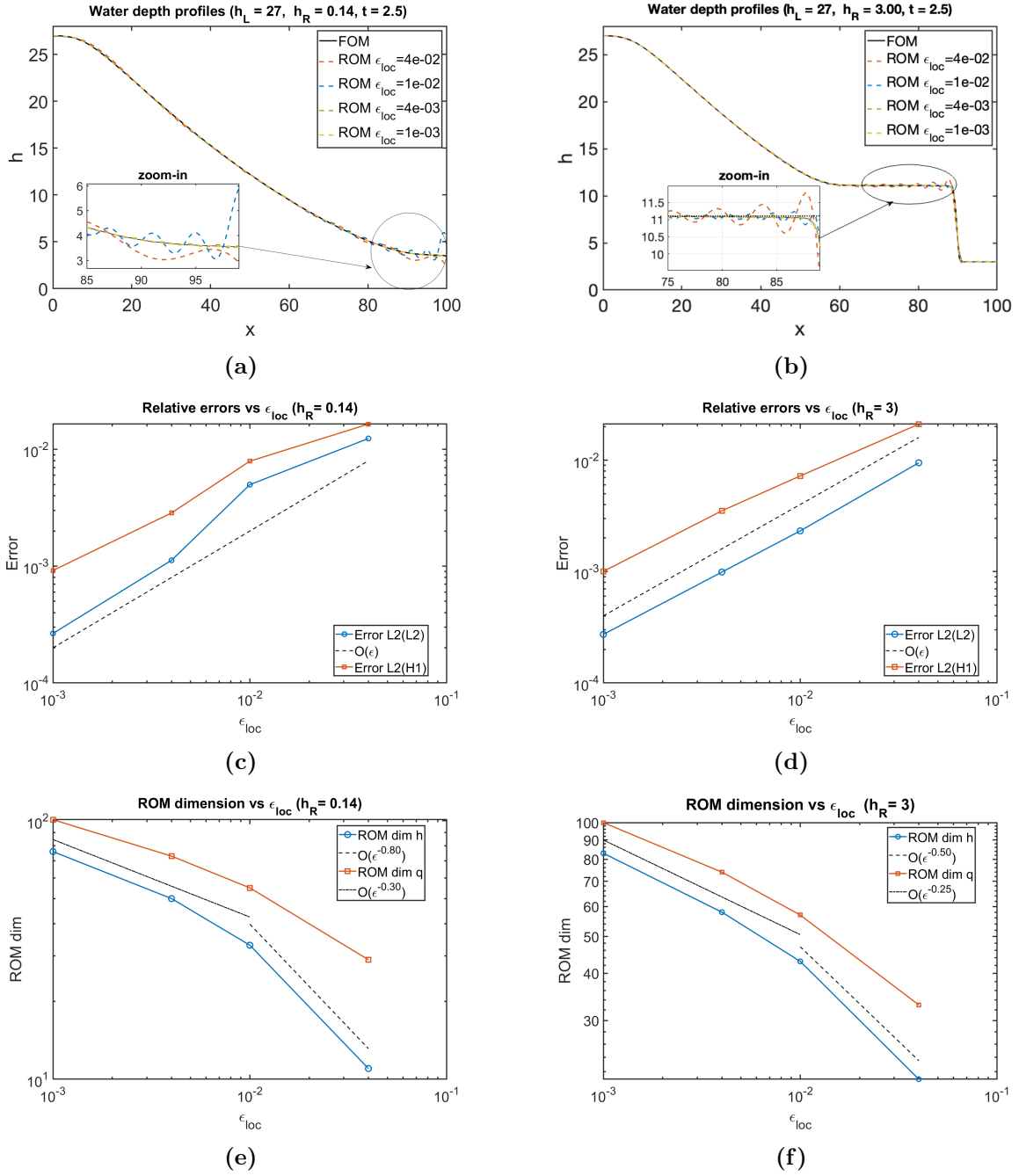


**Figure 2:** Performance metrics for varying the local threshold  $\epsilon_{loc}$  (from  $4.0 \times 10^{-2}$  to  $1.0 \times 10^{-3}$ ) in the non-interpolatory tROM ( $h_L = 27$  m): (a) water depth profiles at final time for  $h_R = 0.14$  m, with a zoom-in of the step region showing improved shock front resolution as  $\epsilon_{loc}$  decreases; (b) water depth profiles at final time for  $h_R = 3.00$  m, with a zoom-in of the step region indicating smoother transitions but similar trends; (c) relative errors in  $h$  versus the local threshold with  $h_R = 0.14$  m; (d) relative errors in  $h$  versus the local threshold with  $h_R = 3.00$  m, exhibiting a similar error reduction trend; (e) ROM dimensions ( $\ell_h, \ell_q$ ) for  $h_R = 0.14$  m, increasing with smaller  $\epsilon_{loc}$  to retain more basis vectors; (f) ROM dimensions ( $\ell_h, \ell_q$ ) for  $h_R = 3.00$  m, also increasing with smaller  $\epsilon_{loc}$ .

$h_R$	$E_{L^2(L^2)}(\boldsymbol{\mu})$		$E_{L^2(H^1)}(\boldsymbol{\mu})$		$\ell_h$		$\ell_q$	
	a	f	a	f	a	f	a	f
0	$1.59 \times 10^{-3}$	$1.28 \times 10^{-4}$	$2.52 \times 10^{-3}$	$2.59 \times 10^{-4}$	15	30	23	50
0.02	$2.51 \times 10^{-3}$	$3.41 \times 10^{-3}$	$3.74 \times 10^{-3}$	$4.82 \times 10^{-3}$	34	30	55	50
0.07	$6.87 \times 10^{-4}$	$7.58 \times 10^{-3}$	$1.71 \times 10^{-3}$	$1.10 \times 10^{-2}$	51	30	74	50
0.5	$8.01 \times 10^{-4}$	$4.50 \times 10^{-3}$	$2.84 \times 10^{-3}$	$1.07 \times 10^{-2}$	64	30	79	50
1	$8.05 \times 10^{-4}$	$5.08 \times 10^{-3}$	$2.84 \times 10^{-3}$	$1.26 \times 10^{-2}$	65	30	80	50
2	$8.58 \times 10^{-4}$	$5.04 \times 10^{-3}$	$3.25 \times 10^{-3}$	$1.36 \times 10^{-2}$	61	30	78	50
3	$9.61 \times 10^{-4}$	$4.79 \times 10^{-3}$	$3.49 \times 10^{-3}$	$1.31 \times 10^{-2}$	56	30	71	50
5	$9.81 \times 10^{-4}$	$3.94 \times 10^{-3}$	$3.45 \times 10^{-3}$	$1.07 \times 10^{-2}$	49	30	62	50
7	$9.72 \times 10^{-4}$	$3.23 \times 10^{-3}$	$2.95 \times 10^{-3}$	$8.20 \times 10^{-3}$	45	30	57	50

**Table 2:** Adaptive <sup>(a)</sup> versus fixed-dimension <sup>(f)</sup> ROM errors and dimensions for varying  $h_R$  ( $h_L = 25$ ,  $\epsilon_{\text{loc}} = 4.0 \times 10^{-3}$ ; fixed dimensions:  $\ell_h = 30$ ,  $\ell_q = 50$ ).

increasing as  $h_R$  decreases, reaching a maximum before dropping to their minima at  $h_R = 0$ . In the case of fixed ROM dimensions, the errors remain very stable over the entire range of  $h_R$ , with the highest accuracy achieved for the dry-bed scenario. These results indicate that tROMs can successfully handle the challenging case  $h_R \rightarrow 0$ . In particular, tROMs with both adaptive and fixed dimensions do not result in a sharp error increase as  $h_R \rightarrow 0$ .

From the results we conclude that the tROM maintains consistent accuracy across varying  $h_R$  values. Adaptive ROM dimensions tend to decrease as  $h_R$  increases, due to the increasingly smooth behavior of the solution. In contrast, fixed ROM dimensions yield higher errors – particularly for small  $h_R$  – indicating that adaptive basis truncation better captures solution variability. This suggests that adaptive ROM dimension selection is more effective across varying flow regimes and will be our default choice for the rest of the paper.

### 3.1.3 Impact of Parameter Grid Distribution for $h_R$

The 1D dam-break problem with a wet bed exhibits singular behavior as the wet-bed depth approaches zero; see the Appendix section. This motivates grid refinement near  $h_R = 0$ . To address this, we compare tROM performance using Chebyshev and uniformly distributed nodes over  $[0, h_R^{\text{max}}]$ .

We assess the effect of node distribution on tROM accuracy and ROM dimensions by varying the number of nodes  $N_R \in \{5, 9, 17\}$  for  $h_R \in [0, 8]$ , while fixing  $N_L = 13$  for  $h_L \in [10, 28]$ . In the offline phase, the  $(N_L, N_R)$  grid defines the training set. In the online phase, we fix  $h_L = 25$  m,  $\epsilon_{\text{loc}} = 4.0 \times 10^{-3}$ , and evaluate performance over 80  $h_R$  values in  $[0, 8]$ .

We compute aggregate error metrics across these 80 points, along with mean and maximum ROM dimensions  $(\ell_h, \ell_q)$ . Results are summarized in Table 4. To highlight differences, we plot water-depth evolution and relative errors for selected cases with  $N_L = 13$ ,  $N_R = 9$ ,  $h_L = 25$  m, and  $h_R \in \{0.05, 0.3\}$  m (see Figure 3).

The key finding is that Chebyshev nodes consistently outperform uniform ones, yielding lower errors across all  $N_R$ . Uniform grids underperform near small  $h_R$ , where solution discontinuities dominate, leading to increased errors (Figures 3c and 3d). Chebyshev nodes, by clustering points near  $h_R = 0$ , better resolve these features and improve both accuracy and stability in the non-interpolatory tROM.

$N_R$	tROM type	$E_{L^2(L^2)}^{\text{sup}}(h_L)$	$E_{L^2(L^2)}^{\text{avr}}(h_L)$	$E_{L^2(H^1)}^{\text{sup}}(h_L)$	$E_{L^2(H^1)}^{\text{avr}}(h_L)$	Mean $\ell_h$	Mean $\ell_q$	Max $\ell_h$	Max $\ell_q$
5	Chebyshev	$3.48 \times 10^{-3}$	$1.14 \times 10^{-2}$	$5.91 \times 10^{-3}$	$2.83 \times 10^{-2}$	57	73	70	85
5	Uniform	$6.67 \times 10^{-3}$	$1.33 \times 10^{-2}$	$1.02 \times 10^{-2}$	$3.65 \times 10^{-2}$	55	71	64	83
9	Chebyshev	$1.60 \times 10^{-3}$	$7.62 \times 10^{-3}$	$3.72 \times 10^{-3}$	$2.50 \times 10^{-2}$	55	70	68	89
9	Uniform	$5.15 \times 10^{-3}$	$9.16 \times 10^{-3}$	$7.94 \times 10^{-3}$	$3.17 \times 10^{-2}$	54	69	67	85
17	Chebyshev	$1.60 \times 10^{-3}$	$7.51 \times 10^{-3}$	$3.54 \times 10^{-3}$	$2.53 \times 10^{-2}$	52	67	65	86
17	Uniform	$2.92 \times 10^{-3}$	$8.05 \times 10^{-3}$	$5.10 \times 10^{-3}$	$3.08 \times 10^{-2}$	52	67	65	85

**Table 4:** Comparison of Chebyshev vs. uniform node distributions for varying  $N_R$  ( $h_L = 25$ ,  $\epsilon_{\text{loc}} = 4.0 \times 10^{-3}$ ).

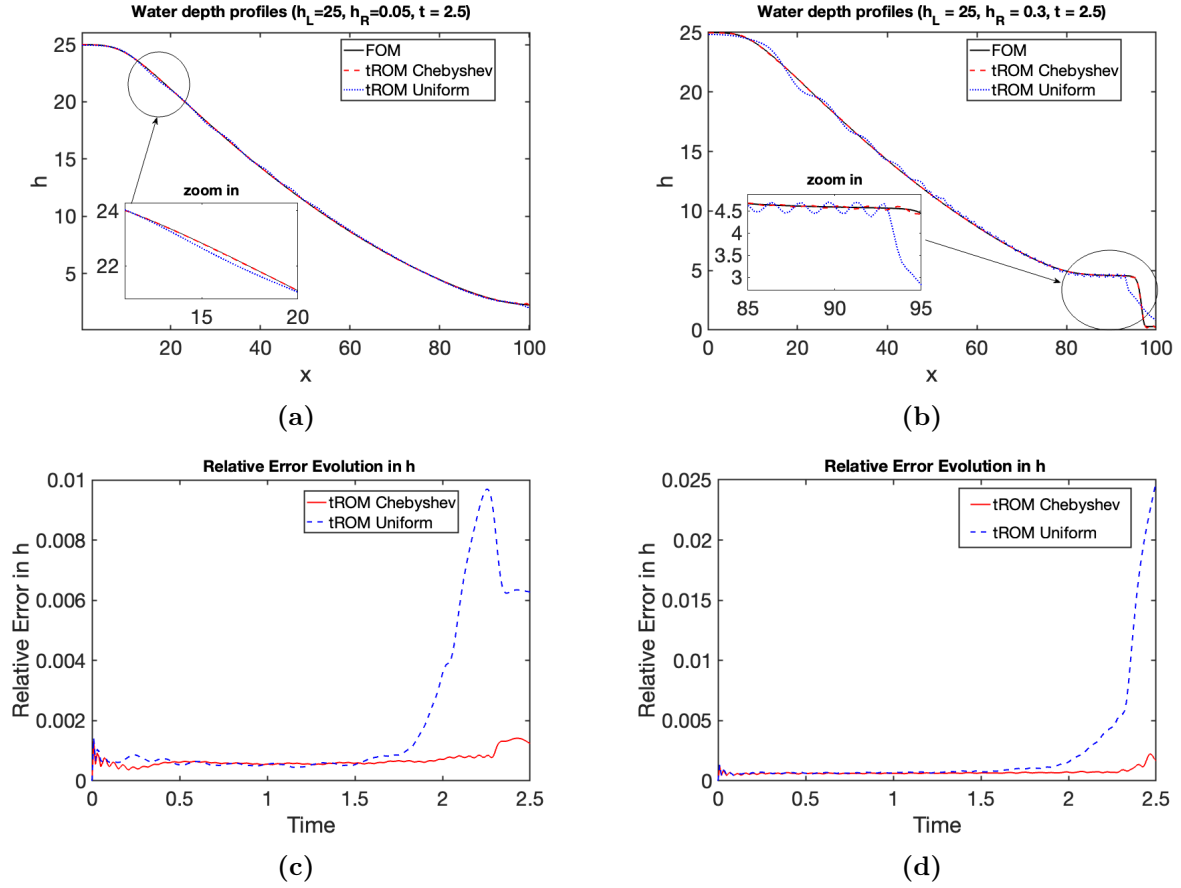


**Figure 3:** Comparison of water depth profiles and relative  $L^2$  errors for  $h_L = 25$  m using Chebyshev and uniform node distributions ( $N_L = 13$ ,  $N_R = 9$ ) in the non-interpolatory tROM: (a) final-time depth profiles for  $h_R = 0.05$  m; (b) final-time depth profiles for  $h_R = 0.3$  m; (c) relative  $L^2(0, T; L^2(\Omega))$  error over time for  $h_R = 0.05$  m; (d) same error metric for  $h_R = 0.3$  m.

$N_R$	tROM type	$E_{L^2(L^2)}^{\text{sup}}(h_L)$	$E_{L^2(L^2)}^{\text{avr}}(h_L)$	$E_{L^2(H^1)}^{\text{sup}}(h_L)$	$E_{L^2(H^1)}^{\text{avr}}(h_L)$	Mean $\ell_h$	Mean $\ell_q$	Max $\ell_h$	Max $\ell_q$
5	Interpolatory	$2.08 \times 10^{-2}$	$2.86 \times 10^{-2}$	$3.26 \times 10^{-2}$	$5.75 \times 10^{-2}$	43	56	53	70
5	Non-interpolatory	$3.48 \times 10^{-3}$	$1.14 \times 10^{-2}$	$5.91 \times 10^{-3}$	$2.83 \times 10^{-2}$	57	73	70	85
9	Interpolatory	$1.02 \times 10^{-2}$	$1.47 \times 10^{-2}$	$1.78 \times 10^{-2}$	$4.10 \times 10^{-2}$	43	56	53	70
9	Non-interpolatory	$1.60 \times 10^{-3}$	$7.62 \times 10^{-3}$	$3.72 \times 10^{-3}$	$2.50 \times 10^{-2}$	55	70	68	89
17	Interpolatory	$3.40 \times 10^{-3}$	$1.05 \times 10^{-2}$	$8.03 \times 10^{-3}$	$3.43 \times 10^{-2}$	44	56	53	70
17	Non-interpolatory	$1.60 \times 10^{-3}$	$7.51 \times 10^{-3}$	$3.54 \times 10^{-3}$	$2.53 \times 10^{-2}$	52	67	65	85

**Table 5:** Interpolatory vs. non-interpolatory tROMs for varying  $N_R$  ( $h_L = 25$ ,  $\epsilon_{\text{loc}} = 4.0 \times 10^{-3}$ ).

$N_L$	$N_R$	ROM Type	$E_{L^2(L^2)}^{\text{sup}}$	$E_{L^2(L^2)}^{\text{avr}}$	$E_{L^2(H^1)}^{\text{sup}}$	$E_{L^2(H^1)}^{\text{avr}}$	Mean $\ell_h$	Max $\ell_h$	Mean $\ell_q$	Max $\ell_q$
4	5	tROM	$3.32 \times 10^{-3}$	$1.40 \times 10^{-1}$	$6.41 \times 10^{-3}$	$4.16 \times 10^{-1}$	50	72	67	92
4	5	POD	$4.52 \times 10^{-3}$	$3.29 \times 10^{-1}$	$1.09 \times 10^{-2}$	$8.20 \times 10^{-1}$	50	72	67	92
7	9	tROM	$1.47 \times 10^{-3}$	$1.41 \times 10^{-1}$	$4.12 \times 10^{-3}$	$4.33 \times 10^{-1}$	45	70	60	90
7	9	POD	$6.80 \times 10^{-3}$	$4.50 \times 10^{-1}$	$1.11 \times 10^{-2}$	$1.04 \times 10^0$	45	70	60	90
13	17	tROM	$1.53 \times 10^{-3}$	$1.43 \times 10^{-1}$	$3.82 \times 10^{-3}$	$4.48 \times 10^{-1}$	42	66	56	85
13	17	POD	$1.03 \times 10^{-2}$	$5.44 \times 10^{-1}$	$1.36 \times 10^{-2}$	$1.18 \times 10^0$	42	66	56	85
20	25	tROM	$1.35 \times 10^{-3}$	$1.45 \times 10^{-1}$	$3.72 \times 10^{-3}$	$4.55 \times 10^{-1}$	41	65	54	84
20	25	POD	$1.17 \times 10^{-2}$	$5.87 \times 10^{-1}$	$1.44 \times 10^{-2}$	$1.26 \times 10^0$	41	65	54	84

**Table 6:** Comparison of tROM and POD ROM with Monte Carlo sampling for varying  $N_L$  and  $N_R$  ( $\epsilon_{\text{loc}} = 4.0 \times 10^{-3}$ ).

### 3.1.4 Interpolatory vs. Non-Interpolatory tROM

In this experiment, we compare the performance of interpolatory and non-interpolatory tROMs using Chebyshev nodes for the 1D dam-break problem. We fix  $h_L = 25$  m,  $\epsilon_{\text{loc}} = 4.0 \times 10^{-3}$ , and  $N_L = 13$ , and vary  $N_R \in \{5, 9, 17\}$ . In the offline phase,  $N_L$  and  $N_R$  define the parameter grid for  $h_L$  and  $h_R$ , respectively. For each  $(N_L, N_R)$  pair, we generate snapshot data using the FOM, which is then stored for use in the online phase. During the online phase, we evaluate the ROMs over a fine grid in  $h_R \in [0, 8]$ , computing aggregated error metrics (as defined in (3.1)) along with the mean and maximum ROM dimensions ( $\ell_h, \ell_q$ ).

The results are summarized in Table 5. To further illustrate performance differences, we present simulation plots for the specific case  $N_L = 13$ ,  $N_R = 9$ ,  $h_L = 25$  m, and  $h_R \in \{0.05, 2\}$  m, showing the evolution of water depth and relative errors in  $h$  over time (see Figures 4).

We find that the non-interpolatory tROM consistently outperforms the interpolatory tROM across all tested values of  $N_R$ . Although it results in higher ranks, the increased dimensionality enables better resolution of solution variability.

### 3.1.5 tROM vs POD ROM

In this experiment, we compare the performance of the non-interpolatory tROM to that of the POD ROM. We fix  $\epsilon_{\text{loc}} = 4.0 \times 10^{-3}$  and vary the parameter grid sizes with  $N_L \in \{4, 7, 13, 20\}$  and  $N_R \in \{5, 9, 17, 25\}$ . To ensure a consistent comparison, we use the ROM dimensions obtained from the tROM online phase (with  $\epsilon_{\text{loc}} = 4.0 \times 10^{-3}$ ) for both the tROM and the POD ROM. Note that these ROM dimensions may vary depending on the parameter grid used in each simulation.

The results, summarized in Table 6, show that the non-interpolatory tROM consistently outperforms the POD ROM across all tested values of  $N_L$  and  $N_R$ . This improvement is attributed to the tensor structure, which enable the tROM to better adapt to the solution variability across the parameter domain.

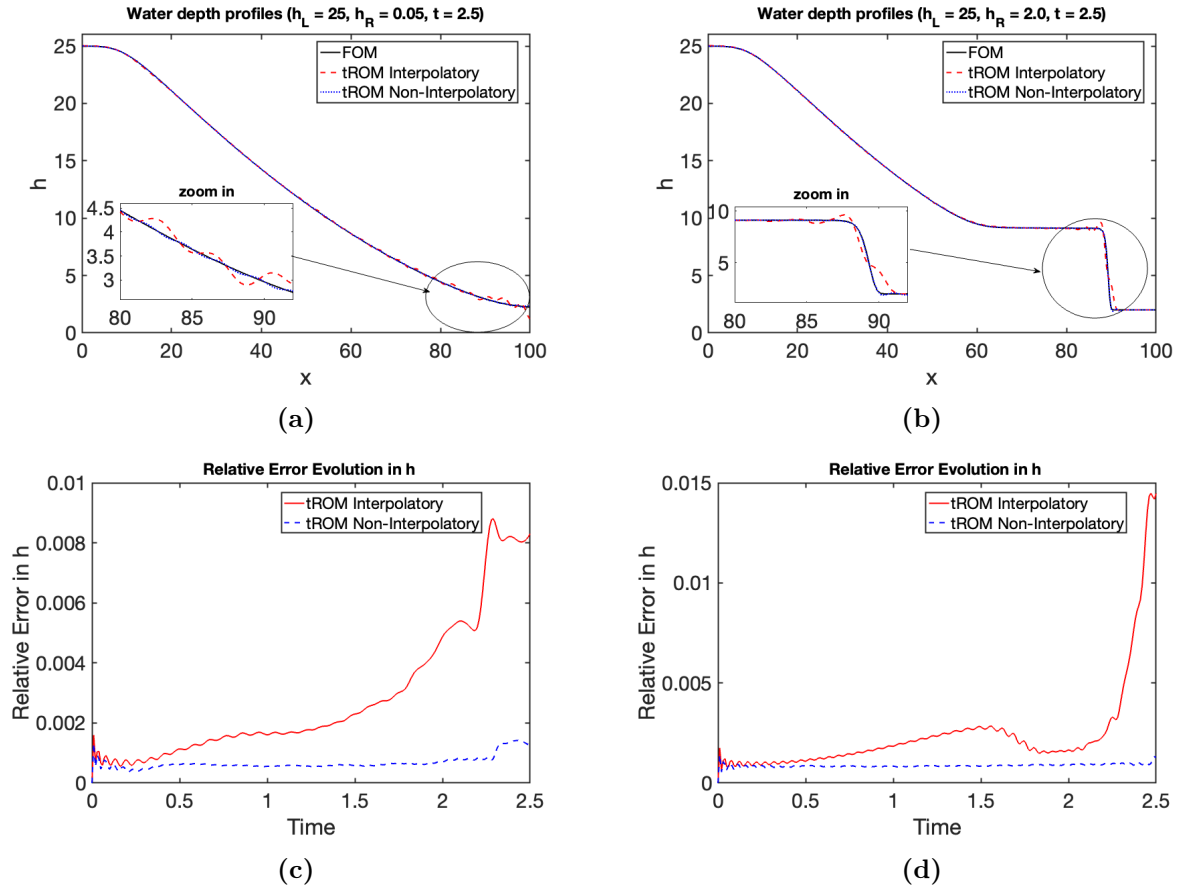


**Figure 4:** Water depth profiles and error evolution over time for specific parameter pairs ( $N_L = 13, N_R = 9, h_L = 25$  m), comparing interpolatory and non-interpolatory tROMs : (a) water depth profiles at final time for  $h_R = 0.05$  m; (b) water depth profiles at final time for  $h_R = 2$  m; (c) relative error evolution in over time for  $h_R = 0.05$  m; (d) relative error evolution over time for  $h_R = 2.00$  m.

$N_L$	$N_R$	ROM Type	$E_{L^2(L^2)}^{\text{sup}}$	$E_{L^2(L^2)}^{\text{avr}}$	$E_{L^2(H^1)}^{\text{sup}}$	$E_{L^2(H^1)}^{\text{avr}}$
4	5	tROM	$7.36 \times 10^{-3}$	$5.53 \times 10^{-1}$	$1.70 \times 10^{-2}$	$1.34 \times 10^0$
4	5	POD	$9.73 \times 10^{-3}$	$9.19 \times 10^{-1}$	$1.83 \times 10^{-2}$	$1.93 \times 10^0$
7	9	tROM	$6.47 \times 10^{-3}$	$4.45 \times 10^{-1}$	$1.55 \times 10^{-2}$	$1.17 \times 10^0$
7	9	POD	$9.55 \times 10^{-3}$	$9.42 \times 10^{-1}$	$1.82 \times 10^{-2}$	$1.93 \times 10^0$
13	17	tROM	$5.68 \times 10^{-3}$	$3.93 \times 10^{-1}$	$1.44 \times 10^{-2}$	$1.06 \times 10^0$
13	17	POD	$9.74 \times 10^{-3}$	$9.44 \times 10^{-1}$	$1.80 \times 10^{-2}$	$1.91 \times 10^0$
20	25	tROM	$5.48 \times 10^{-3}$	$3.72 \times 10^{-1}$	$1.43 \times 10^{-2}$	$1.03 \times 10^0$
20	25	POD	$9.81 \times 10^{-3}$	$9.44 \times 10^{-1}$	$1.80 \times 10^{-2}$	$1.90 \times 10^0$

**Table 7:** Comparison of tROM and POD ROM with Monte Carlo sampling for varying  $N_L$  and  $N_R$ , fixed ROM dimensions  $\ell_h = 30$ ,  $\ell_q = 50$ .

We further compare the non-interpolatory tROM to the POD ROM using fixed ROM dimensions  $\ell_h = 30$  and  $\ell_q = 50$  for both methods, instead of adapting dimensions based on the threshold  $\epsilon_{\text{loc}}$ . We vary the parameter grid sizes with  $N_L \in \{4, 7, 13, 20\}$  and  $N_R \in \{5, 9, 17, 25\}$ . Results, summarized in Table 7, confirm that the non-interpolatory tROM consistently outperforms the POD ROM across all  $N_L$  and  $N_R$  even with fixed ROM dimensions.

Finally, Figures 5 and 6 visualize the water depth profiles at the final time and the evolution of relative errors for parameter pairs  $(h_L, h_R) \in \{(12, 0), (12, 7), (15, 4), (18, 0), (26, 0.14), (26, 7)\}$ , representing a range of flow regimes. Again, we observe that the tROM outperforms the POD ROM in terms of solution accuracy and suppression of spurious oscillations, given that both methods use the same reduced dimensions.

## 4 Conclusions

In this paper, we developed a non-interpolatory variant of the tROM for the parameterized shallow-water dam-break problem. We also investigated the dependence of solutions on the parameters  $(h_L, h_R)$ . This setup presents several challenges specific to hyperbolic problems. First, the dimension of the reduced basis is expected to be relatively high compared to parabolic problems. This is directly linked to the slow decay of the Kolmogorov  $N$ -width in hyperbolic settings. Second, the solution may develop shock waves. Combined with parametric dependence, this necessitates the development of advanced numerical methods for model reduction. We demonstrated that a properly designed tROM can successfully address this challenge and provide accurate approximations of high-fidelity simulations.

Another difficulty is particular to the problem at hand and stems from the behavior of the SWE solutions for small values of  $h_R$ . As shown in the appendix, the derivative of the solution with respect to the second parameter is not uniformly bounded in the neighborhood of  $h_R = 0$ . Consequently, constructing a parametric ROM for the wet-bed problem is especially challenging. The non-interpolatory tROM with adaptive sampling — using Chebyshev nodes to cluster samples near  $h_R = 0$  — effectively addresses this issue and offers an efficient framework for projection-based ROM development. As demonstrated in Section 3.1.2, tROMs with both adaptive and fixed local dimensions can successfully handle the limiting case  $h_R \rightarrow 0$ .

Our results indicate that the novel tROM methodology can successfully handle hyperbolic problems with varying parameters. In particular, tROMs developed in this paper perform very well for a test problem in the regime representing typical behavior of hyperbolic systems. Therefore, we expect that the tROM approach discussed in this paper will also be applicable to more

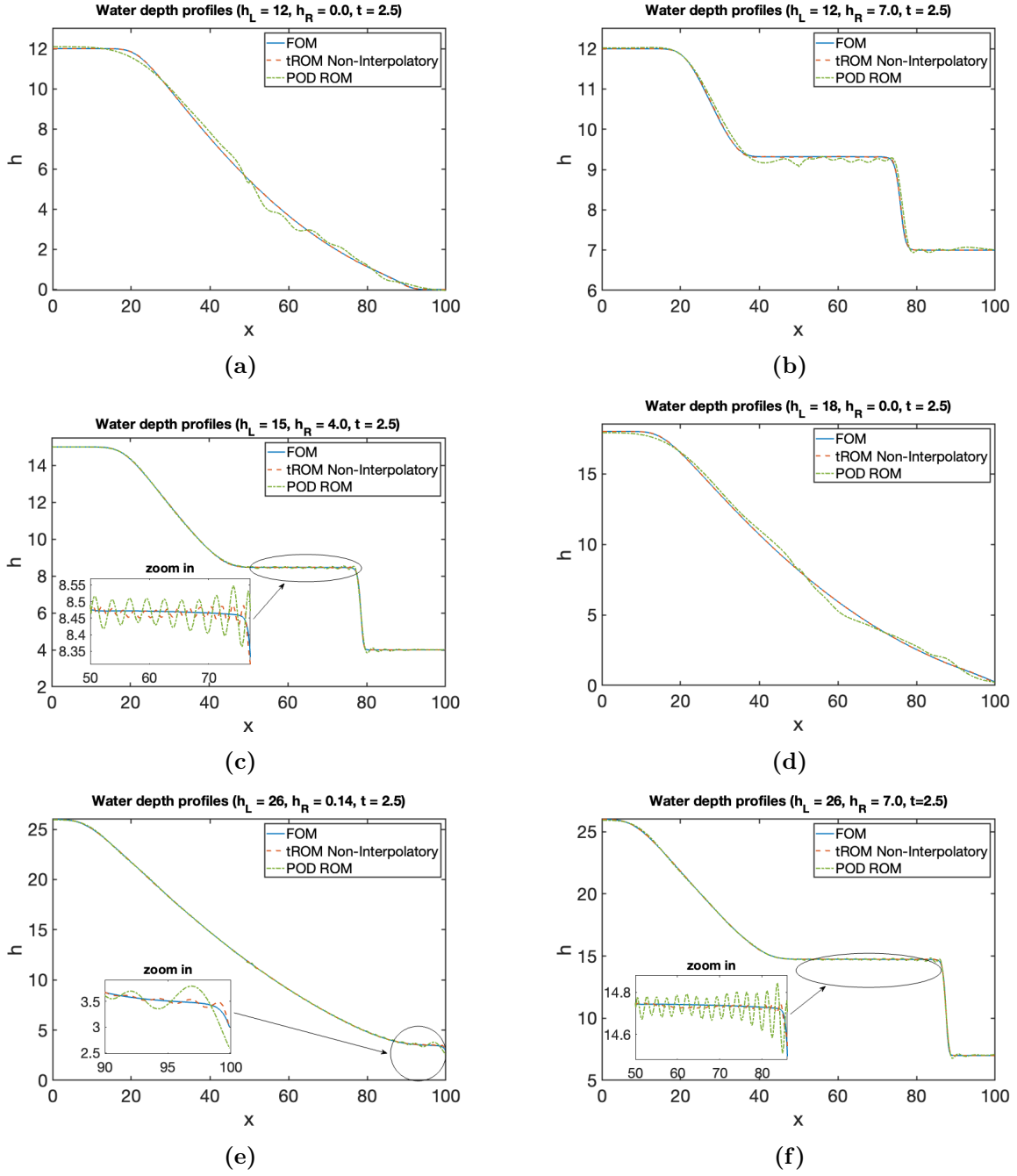


**Figure 5:** Water depth profiles at final time for different parameter pairs, comparing non-interpolatory tROM and POD ROM (with equal ROM dimensions derived from tROM using  $\epsilon_{loc} = 4.0 \times 10^{-3}$ ) with Chebyshev nodes: (a) for  $h_L = 12, h_R = 0$ ; (b) for  $h_L = 12, h_R = 7$ ; (c) for  $h_L = 15, h_R = 4$ ; (d) for  $h_L = 18, h_R = 0$ ; (e) for  $h_L = 26, h_R = 0.14$ ; (f) for  $h_L = 26, h_R = 7$ ; .

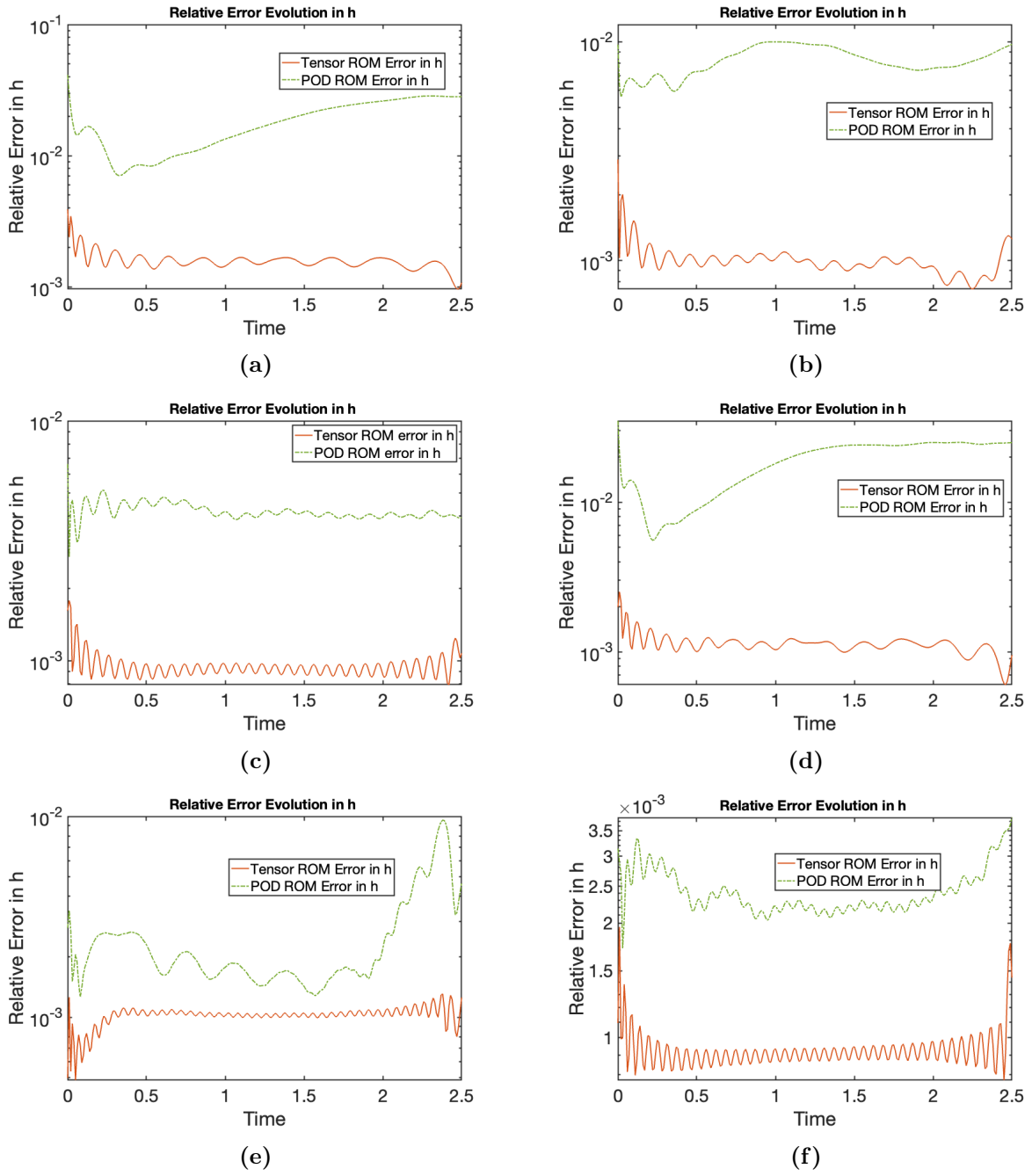


**Figure 6:** Evolution of relative errors in water depth for different parameter pairs, comparing non-interpolatory tROM and POD ROM (with equal ROM dimensions derived from tROM using  $\epsilon_{loc} = 4.0 \times 10^{-3}$ ) with Chebyshev nodes : (a) for  $h_L = 12, h_R = 0$ ; (b) for  $h_L = 12, h_R = 7$ ; (c) for  $h_L = 15, h_R = 4$ ; (d) for  $h_L = 18, h_R = 0$ ; (e) for  $h_L = 26, h_R = 0.14$ ; (f) for  $h_L = 26, h_R = 7$ .

realistic hyperbolic systems in higher dimensions. However, one of the major challenges in the ROM community is developing accurate and efficient projection-based ROMs for problems that involve a relatively high-dimensional vector of parameters. As discussed in our paper, for hyperbolic problems, it might be necessary to perform clustered sampling near certain parameter values; this would present a major challenge if the vector of parameters is high-dimensional. Thus, further development of tensor completion and interpolation techniques might be necessary for problems that require clustered sampling. This will be addressed in forthcoming papers.

## Acknowledgment

The authors R.B.M. and M.O. were supported in part by the U.S. National Science Foundation under awards DMS-2309197 and DMS-2408978.

## A Analytical Solution of the Dam-Break Problem

In this section we recall analytical solutions for the 1D dam-break problem and study the behavior of the wet-bed case solution in the proximity of the dry-bed case. The dam-break problem can be solved analytically for both cases, using a combination of Riemann invariants, Rankine–Hugoniot conditions, and Newton iteration to determine the middle state.

### Dry-Bed Case ( $h_R = 0$ )

For the dry-bed case, where the initial right water height  $h_R = 0$ , the solution consists of a rarefaction wave spreading from the dam location  $x_{\text{dam}}$ . Given an initial left water height  $h_L$ , the solution at time  $t$  and position  $x$  is determined by the characteristic speeds. Let  $c = \sqrt{gh_L}$  be the gravity wave speed on the left side, and  $x_\ell = x_{\text{dam}} - ct$  and  $x_r = x_{\text{dam}} + 2ct$  define the left and the right ends (i.e. the tail and the head) of the rarefaction wave, respectively. The analytical solution for water depth  $h(x, t)$  and velocity  $u(x, t)$  is given by

$$[u(x, t), h(x, t)] = \begin{cases} [0, h_L] & \text{if } x < x_\ell, \\ \left[ \frac{2}{3}(c + \delta), \frac{4}{9g} \left( c - \frac{\delta}{2} \right)^2 \right] & \text{if } x_\ell \leq x \leq x_r, \\ [0, 0] & \text{if } x > x_r, \end{cases} \quad (19)$$

where  $\delta = (x - x_{\text{dam}})/t$ . This solution reflects a rarefaction wave expanding into the dry region, with the water depth decreasing smoothly from  $h_L$  to 0 across the wave.

### Wet-Bed Case ( $h_R > 0$ )

For the wet-bed case, where  $h_R > 0$ , the solution involves a rarefaction wave on the left, a constant middle state  $(h_m, u_m)$ , and a shock wave on the right. The middle state and shock speed  $s$  are determined by solving a system of equations using the Riemann invariant across the left rarefaction wave and the Rankine–Hugoniot conditions. The middle state  $(h_m, u_m)$  and shock speed  $s$  satisfy the nonlinear equation

$$u_m + 2\sqrt{gh_m} - 2\sqrt{gh_L} = 0, \quad (20)$$

where

$$u_m = s - \frac{gh_R}{4s} \left( \sqrt{1 + \frac{8s^2}{gh_R}} + 1 \right), \quad h_m = \frac{h_R}{2} \left( \sqrt{1 + \frac{8s^2}{gh_R}} - 1 \right). \quad (21)$$

The  $s$  solving the above equation can be computed numerically using, for instance, Newton's method. Newton's iteration starts with an initial guess  $s = \sqrt{gh_L}$  and iteratively updates  $s$  until convergence.

Given the middle state, the solution at time  $t$  and position  $x$  is determined by the positions of the rarefaction on wave and shock. The the gravity wave speed  $c$ ,  $\delta$ , and the tail if the wave  $x_1 = x_\ell$  are the same as in the dry case. Let  $c_m = \sqrt{gh_m}$ ,  $x_2 = x_{\text{dam}} + (u_m - c_m)t$ , and  $x_3 = x_{\text{dam}} + st$ . The analytical solution for the wet case is then given by

$$[u(x, t), h(x, t)] = \begin{cases} [0, h_L] & \text{if } x \leq x_1, \\ \left[ \frac{2}{3}(c + \delta), \frac{4}{9g} \left( c - \frac{\delta}{2} \right)^2 \right] & \text{if } x_1 < x < x_2, \\ [u_m, h_m] & \text{if } x_2 \leq x \leq x_3, \\ [0, h_R] & \text{if } x > x_3. \end{cases} \quad (22)$$

This solution captures the rarefaction wave, the constant middle state, and the shock wave propagating to the right.

### Convergence and regularity for $h_R \rightarrow 0$

We are now interested in the behavior of the wet-bed solution when  $h_R \rightarrow 0$ . It is easy to see from the second equation in (21) that  $h_m \sim \sqrt{h_R} \rightarrow 0$ . Then from (20) we obtain  $u_m \rightarrow 2\sqrt{gh_L} = 2c$  also with the speed  $O(\sqrt{h_R})$ . On the other hand, from the first equation in (21),  $u_m \rightarrow s$ . Therefore,  $(h_m, u_m, s) \rightarrow (0, 2c, 2c)$  as  $h_R \rightarrow 0$ . We also have  $x_3 \rightarrow x_r$  and  $x_2 \rightarrow x_r$  as  $h_R \rightarrow 0$ . Therefore, the solution of the wet-bed converges in  $L^\infty(0, L)$  to the solution of the dry-bed as  $h_R \rightarrow 0$  uniformly in time  $t \in [0, T]$  if  $x_{\text{dam}} + 2cT < L$ . However, the solution of the wet-bed is not differentiable for any  $t > 0$  because the shock appears immediately, since  $x_3 - x_2 > 0$  for any  $t > 0$ . This is evident since  $s - u_m > 0$  for any  $h_R > 0$  (the first equation in (21)) and  $c_m$  is also strictly positive for  $h_R > 0$ . Thus, although there is convergence in  $L^\infty(0, L)$ , the wet-bed solutions fail to converge to the dry-bed solution in  $H^1(0, L)$  norm for  $h_R \rightarrow 0$  and any fixed  $t > 0$ .

We are also interested in the regularity of the wet-bed case solution with respect the  $h_R$  parameter in the proximity of  $h_R = 0$ . First note that  $s \rightarrow c > 0$  as  $h_R \rightarrow 0$  and so the propagation speed of the shock is uniformly bounded away from zero. For  $x \in (x_2, x_3)$  the water depth is given by  $h = h_m$  and from (21) we obtain  $\partial h / \partial h_R \sim O(h_R^{-\frac{1}{2}})$  on  $(x_2, x_3)$  for small  $h_R$ . The interval length is  $x_3 - x_2 = (s - u_m + c_m)t \sim O(h_R^{1/4})t$ , since  $s - u_m \geq 0$ ,  $c_m = \sqrt{gh_m}$  and  $h_m \sim O(h_R^{\frac{1}{2}})$ . We conclude that the derivative of  $\partial h(x, t) / \partial h_R$  is unbounded on  $(0, L)$  when  $h_R \rightarrow 0$  and for any  $t > 0$ . More generally, straightforward calculations show that the  $L^p(0, L)$  norm of  $\partial h / \partial h_R$  has  $O(h_R^{\frac{1}{4p} - \frac{1}{2}})$  asymptotic for  $h_R \rightarrow 0$ . Furthermore, similar calculations shows the same asymptotics for  $\partial u(x, t) / \partial h_R$  and for  $\partial q(x, t) / \partial h_R$  in the neighborhood of the dry-bed case.

## References

- [1] R. Abgrall and R. Crisovan. Model reduction using L1-norm minimization as an application to nonlinear hyperbolic problems. *International Journal for Numerical Methods in Fluids*, 87(12):628–651, 2018.

- [2] M. Bachmayr and A. Cohen. Kolmogorov widths and low-rank approximations of parametric elliptic pdes. *Mathematics of Computation*, 86(304):701–724, 2017.
- [3] P. Benner, S. Gugercin, and K. Willcox. A survey of projection-based model reduction methods for parametric dynamical systems. *SIAM review*, 57(4):483–531, 2015.
- [4] A. Bihlo and R. O. Popovych. Physics-informed neural networks for the shallow-water equations on the sphere. *Journal of Computational Physics*, 456:111024, 2022.
- [5] P. Binev, A. Cohen, W. Dahmen, R. DeVore, G. Petrova, and P. Wojtaszczyk. Convergence rates for greedy algorithms in reduced basis methods. *SIAM Journal on Mathematical Analysis*, 43(3):1457–1472, 2011.
- [6] A. Buffa, Y. Maday, A. T. Patera, C. Prud’Homme, and G. Turinici. A priori convergence of the greedy algorithm for the parametrized reduced basis method. *ESAIM: Mathematical modelling and numerical analysis*, 46(3):595–603, 2012.
- [7] J. Chan. Entropy stable reduced order modeling of nonlinear conservation laws. *Journal of Computational Physics*, 423:109789, 2020.
- [8] T.-J. Chang, H.-M. Kao, K.-H. Chang, and M.-H. Hsu. Numerical simulation of shallow-water dam break flows in open channels using smoothed particle hydrodynamics. *Journal of Hydrology*, 408(1-2):78–90, 2011.
- [9] A. Cohen and R. DeVore. Kolmogorov widths under holomorphic mappings. *IMA Journal of Numerical Analysis*, 36(1):1–12, 2016.
- [10] A. Cohen, R. DeVore, and C. Schwab. Convergence rates of best n-term Galerkin approximations for a class of elliptic pdes. *Foundations of Computational Mathematics*, 10(6):615–646, 2010.
- [11] R. Crisovan, D. Torlo, R. Abgrall, and S. Tokareva. Model order reduction for parametrized nonlinear hyperbolic problems as an application to uncertainty quantification. *Journal of Computational and Applied Mathematics*, 348:466–489, 2019.
- [12] C. Greif and K. Urban. Decay of the Kolmogorov N-width for wave problems. *Applied Mathematics Letters*, 96:216–222, 2019.
- [13] J. S. Hesthaven, G. Rozza, B. Stamm, et al. *Certified reduced basis methods for parametrized partial differential equations*, volume 590. Springer, 2016.
- [14] T. Lassila, A. Manzoni, A. Quarteroni, and G. Rozza. Generalized reduced basis methods and n-width estimates for the approximation of the solution manifold of parametric pdes. *Analysis and numerics of partial differential equations*, pages 307–329, 2013.
- [15] I. Magdalena and M. F. E. Pebriansyah. Numerical treatment of finite difference method for solving dam break model on a wet-dry bed with an obstacle. *Results in Engineering*, 14:100382, 2022.
- [16] A. V. Mamonov and M. A. Olshanskii. Interpolatory tensorial reduced order models for parametric dynamical systems. *Computer Methods in Applied Mechanics and Engineering*, 397:115122, 2022.
- [17] A. V. Mamonov and M. A. Olshanskii. Tensorial parametric model order reduction of nonlinear dynamical systems. *SIAM Journal on Scientific Computing*, 46(3):A1850–A1878, 2024.
- [18] A. V. Mamonov and M. A. Olshanskii. A priori analysis of a tensor ROM for parameter dependent parabolic problems. *SIAM Journal on Numerical Analysis*, 63(1):239–261, 2025.

- [19] J. M. Melenk. On n-widths for elliptic problems. *Journal of mathematical analysis and applications*, 247(1):272–289, 2000.
- [20] D. K. Muchiri, J. N. Hewett, M. Sellier, M. Moyers-Gonzalez, and J. Monnier. Numerical simulations of dam-break flows of viscoplastic fluids via shallow water equations. *Theoretical and Computational Fluid Dynamics*, 38(4):557–581, 2024.
- [21] M. Ohlberger and S. Rave. Reduced basis methods: Success, limitations and future challenges. *arXiv preprint arXiv:1511.02021*, 2015.
- [22] M. A. Olshanskii and L. G. Rebholz. Approximating a branch of solutions to the Navier–Stokes equations by reduced-order modeling. *Journal of Computational Physics*, 524:113728, 2025.
- [23] S.-H. Peng. 1d and 2d numerical modeling for solving dam-break flow problems using finite volume method. *Journal of Applied Mathematics*, 2012(1):489269, 2012.
- [24] X. Qi, G. A. de Almeida, and S. Maldonado. Physics-informed neural networks for solving flow problems modeled by the 2D shallow water equations without labeled data. *Journal of Hydrology*, 636:131263, 2024.
- [25] I. Timofeyev, A. Schwarzmann, and D. Kuzmin. Application of machine learning and convex limiting to subgrid flux modeling in the shallow-water equations. *Mathematics and Computers in Simulation*, 238:163–178, 2025.
- [26] J.-M. Zokagoa and A. Soulaïmani. A pod-based reduced-order model for free surface shallow water flows over real bathymetries for monte-carlo-type applications. *Computer methods in applied mechanics and engineering*, 221:1–23, 2012.
- [27] C. Zoppou and S. Roberts. Numerical solution of the two-dimensional unsteady dam break. *Applied Mathematical Modelling*, 24(7):457–475, 2000.